

# Acceleration and Parallelization Methods for ISRS EGN Model

Ruiyang Xia, Guanjun Gao, Zanshan Zhao, Haoyu Wang, Kun Wen, and Daobin Wang

**Abstract**—The enhanced Gaussian noise (EGN) model, which accounts for inter-channel stimulated Raman scattering (ISRS), has been extensively utilized for evaluating nonlinear interference (NLI) within the C+L band. Compared to closed-form expressions and machine learning-based NLI evaluation models, it demonstrates broader applicability and its accuracy is not dependent on the support of large-scale datasets. However, its high computational complexity often results in lengthy computation times. Through analysis, the high-frequency oscillations of the four-wave mixing (FWM) efficiency factor integrand were identified as a primary factor limiting the computational speed of the ISRS EGN model. To address this issue, we propose an accurate approximation method that enables the derivation of a closed-form expression for the FWM efficiency factor without imposing restrictive conditions. Thereby, the scheme proposed in this paper could significantly accelerate the computational speed. Numerical results demonstrate that method in this work could achieve low error levels under high ISRS influence levels, with an MAE of less than 0.001 dB, and no cumulative error over increasing transmission distances, while reducing computation time by over 97%. Furthermore, a parallel computation strategy targeting independent regions within the integration domain is proposed, which could further improve computational efficiency by nearly 11 times.

**Index Terms**—Inter-channel Stimulated Raman Scattering, Enhanced Gaussian Noise model, Closed-Form, Nonlinear interference, Parallel Computation

## I. INTRODUCTION

As modern optical communication systems evolve toward ultra-wideband transmission, nonlinear effects in optical fibers have become increasingly complex and prominent[1-2]. For optical networks with large number

of optical add-drop multiplexer (OADM) nodes and flexibly switched optical wavelength channels, accurate and time-efficient quality of transmission (QoT) estimation becomes extremely important[3-5]. However, brute-force numerical approaches, such as solving the nonlinear Schrödinger equation (NLSE) using the split-step Fourier method (SSFM), are no longer practical due to their high computational complexity[6-7]. The advancement of coherent optical communication with digital signal processing (DSP) has driven the development of the Gaussian noise (GN) model, which models nonlinear noise in uncompensated transmission (UT) as approximately Gaussian[8-11]. Although the GN model provides a relatively efficient method for nonlinear evaluation, it does not account for modulation format effects[12], and several studies have indicated that it may overestimate nonlinear interference (NLI)[13-16]. In 2013, Carena A. et al. proposed the enhanced Gaussian noise (EGN) model by introducing some additional correction terms into the GN model. The EGN model accounts for the modulation format dependence of NLI, thereby offering a more precise assessment of NLI[17]. However, the inter-channel power transfer caused by inter-channel stimulated Raman scattering (ISRS) was not considered in the [17], which cannot be neglected in C+L band transmission scenarios[18]. In 2020, Rabbani H. et al. expanded upon the results [17] by incorporating the interaction between the Kerr effect and ISRS. Additionally, they extended the study to various wavelength division multiplexing (WDM) channel configurations with flexible modulation formats, variable symbol rates, heterogeneous fiber segments, and non-uniform power distributions[19]. The scheme proposed in the [19] could provide more accurate NLI evaluation with broad applicability, but its computational complexity is significantly higher than that of the conventional GN model. Despite its relative speed advantage over SSFM. For scenarios that require real-time evaluation of transmission performance quality, e.g., digital twins, computation time remains a serious issue.

Moreover, many efforts have also been made to further reduce the computation time of the GN or EGN models, resulting in the development of closed-form expressions capable of producing results within picoseconds. In 2017, Semrau D. et al. first derived a closed-form expression for the GN model that accounts for ISRS effects[20]. In 2019, this initial work was extended to incorporate dispersion slope effects and to support arbitrary launch power distributions[21]. Subsequently, this team introduced the effects of cross-phase modulation (XPM), allowing for the consideration of various modulation formats[22].

This work was supported in part by National Key Research and Development Program of China (2022YFB2903303) and National Natural Science Foundation of China (No. 62141505, 61367007 and 62371064); (Corresponding author: Guanjun Gao; Daobin Wang).

Ruiyang Xia, Daobin Wang, and Kun Wen are with the School of Science, Lanzhou University of Technology, Lanzhou 730050, China (e-mail: 232080901001@lut.edu.cn; cougarlz@lut.edu.cn; 1507996369@qq.com)

Guanjun Gao, Zanshan Zhao, and Haoyu Wang are with the School of Electronic Engineering, Beijing University of Posts and Telecommunications, Beijing 100876, China (e-mail: ggj@bupt.edu.cn; zzs@bupt.edu.cn; buptwhy@bupt.edu.cn)

Color versions of one or more of the figures in this article are available online at <http://ieeexplore.ieee.org>

To develop a real-time NLI evaluation model with sufficient accuracy, researchers have explored machine learning techniques, either to improve the accuracy of closed-form expressions or to construct data-driven versions of the EGN model. In 2020, Zefreh M. R. et al. utilized machine learning to refine the incoherent GN closed-form expression[23]. The optimized closed-form expression (CFM2) demonstrated accuracy comparable to the EGN model on the test set. In 2021, Müller J. et al. trained an artificial neural network (ANN) for NLI estimation[24]. In field measurement data, this model provided real-time results with a maximum signal-to-noise ratio (SNR) error of less than 0.5 dB. In 2022, Müller J. et al. used the self-channel interference (SCI) results calculated by the EGN model, along with relevant system parameters, as inputs to an Extreme Gradient Boosting (XGB) algorithm to obtain NLI predictions. [25]. Since it only requires integration over a narrow frequency band, it is faster than using the full EGN model. [24]-[26] used the EGN model to generate data for machine learning applications and achieved effective results in specific optical fiber link configurations.

Although the aforementioned closed-form expressions and machine learning-based approaches offer better real-time performance, the ISRS EGN model is still widely used in many practical applications. On one hand, the ISRS EGN model, free from some restrictive approximation conditions, provides accurate NLI evaluation results across a wide range of application scenarios[26]. On the other hand, the reliability of the ISRS EGN model does not depend on the scale or quality of training data and is not affected by challenges related to generalization[27-29]. To address the issue of slow computation speed in the ISRS EGN model, this work proposes an accurate and efficient acceleration method. Specifically, the contributions of this work are as follows:

(1) A parallel NLI computation method for the independent regions within the ISRS EGN integration domain is proposed, achieving nearly an 11-fold increase in computational efficiency;

(2) Through analysis and numerical validation, the primary factor limiting the computation speed of the ISRS EGN model is identified as the high-frequency oscillations in the integrand of the four-wave mixing (FWM) efficiency factor, which have a more pronounced effect on edge channels;

(3) A closed-form FWM efficiency factor that accounts for ISRS effects is derived, providing reliable results in scenarios with strong ISRS influence and saving over 97% of computation time with an MAE of less than 0.001 dB.

The remainder of this paper is organized as follows. Section II first introduces the overall strategy, followed by detailed descriptions of the proposed parallel acceleration method and the closed-form FWM efficiency factor. Section III evaluates the performance of the proposed acceleration methods and provides discussions. Finally, Section IV concludes the paper.

## II. THE ACCELERATION METHODS

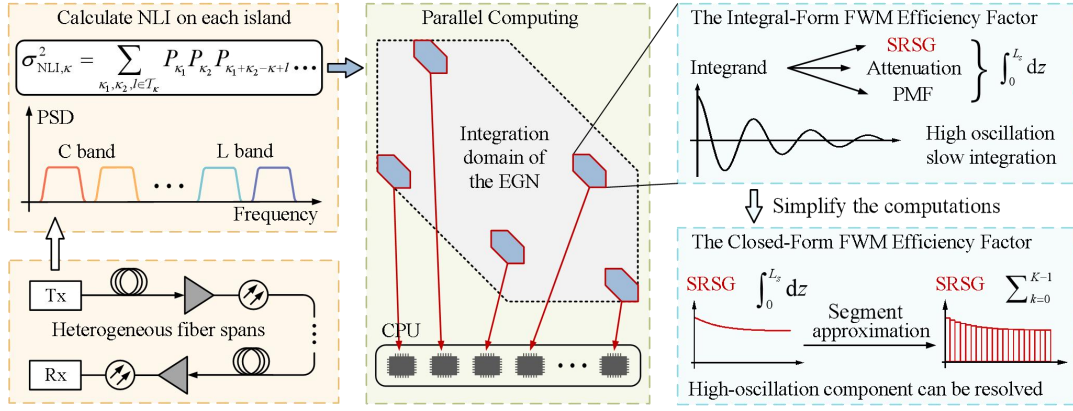
### A. Overall Acceleration Schematic

Fig. 1 illustrates the overall schematic of the proposed ISRS EGN model acceleration method. The base model utilized in this work was introduced in [19], with the relevant equations provided in Appendix B as Eqs. (15)-(25). This model accounts for the combined effects of SCI, cross-channel interference (XCI), multi-channel interference (MCI), and ISRS, enabling accurate NLI evaluation in heterogeneous fiber links over the C+L band. In Eq. (15), the model's integration domain is divided into multiple independent regions, also referred to as "islands", by parameters  $\kappa_1$ ,  $\kappa_2$ , and  $l$ , on which computations are performed independently. The first acceleration method proposed in this work implements parallel computation across these independent islands, as detailed in section B of part II. This strategy significantly enhances computational efficiency without affecting the accuracy of the results.

Furthermore, an analysis of the high computation time issue of the ISRS EGN model revealed that the integral operation in the FWM efficiency factor constitutes the primary bottleneck. By decomposing the integrand, we identified three components: the high-frequency oscillation term, known as the phase mismatch factor (PMF), and two relatively stable terms, the attenuation and stimulated Raman scattering gain (SRSG). By approximating the SRSG, the remaining high-frequency oscillatory component can be directly solved, yielding a closed-form expression for the FWM efficiency factor. Further details are provided in section C of part II.

### B. The Parallel Computing Method

In the ISRS EGN model, for a channel of interest (COI), also referred to as the channel under test (CUT), it is essential to consider the nonlinear interference from all interfering (INT) channels. In the following discussion, to avoid confusion with the frequencies  $f_1$ ,  $f_2$ ,  $f$  within the channel bandwidth in Eqs. (17)-(21), the total frequencies within the WDM bandwidth are denoted as  $f_1^{tot} = f_1 + k_1R$ ,  $f_2^{tot} = f_2 + k_2R$ , and  $f^{tot} = f + kR$ . When  $f^{tot} = 0$ , the integration domain of the ISRS EGN model forms a diamond-shaped structure consisting of multiple islands, as shown in Fig. 2 for the seven-channel case. To facilitate explanation, we take a simplified case with  $B_{ch} \leq 2/3\Delta f$  for example, in which  $B_{ch}$  represents the bandwidth of a single channel and  $\Delta f$  represents the channel spacing. The integration domain can be categorized into SCI, XCI, and MCI according to NLI types: SCI refers to interference caused by nonlinear effects within the COI itself, XCI refers to interference on the COI from one INT channel, and MCI refers to interference on the COI from two or three INT channels[30].



**Fig. 1.** Illustrative diagram of ISRS EGN model acceleration scheme in C+L band heterogeneous optical fiber links, including parallel computation and closed-form FWM efficiency factor.

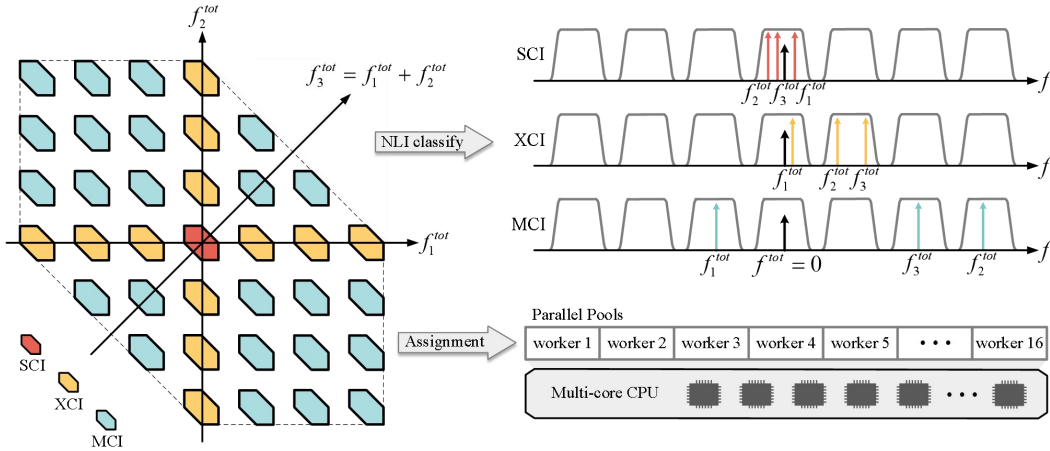


**Fig. 2.** The integration domain of the EGN model consists of numerous islands, with independent calculations on each island. Parallel computation is employed to enhance computational efficiency.

In the ISRS EGN model, integration computations are performed separately across all islands, with computations for each island being independent, making them well-suited for parallel processing. We established a parallel pool consisting of 16 workers within the program. MATLAB's parallel framework automatically assigns computation tasks to workers in the parallel pool and coordinates their execution, while the operating system scheduler manages CPU core allocation, mapping each worker to an available CPU core[31]. The  $P_{NLI}$  computation results for each island are stored in an array, and a summation operation is conducted once all results have been computed. It should be noted that the computational load across islands is inherently unbalanced, which may result in some workers running for extended periods while others remain idle during parallel computation. To address this issue, programs employing the integral-form FWM efficiency factor adopt smaller task block sizes, thereby enhancing allocation granularity and achieving a more balanced load distribution. In contrast, for programs using the closed-form FWM efficiency factor, larger task blocks are employed to reduce communication and synchronization overhead, as these computations are relatively simple[32].

### C. The Closed-Form FWM Efficiency Factor

The FWM efficiency factor quantifies the efficiency of non-degenerate FWM occurring among signals with frequencies  $f_1^{tot}$ ,  $f_2^{tot}$ , and  $f_1^{tot} + f_2^{tot} - f_3^{tot}$  [17]. It is calculated by dividing Eq. (23) by the effective length  $L_{eff}$ . Channels with a smaller absolute value of  $(f_1^{tot} - f_3^{tot}) \cdot (f_2^{tot} - f_3^{tot})$  exhibit higher efficiency in generating FWM effects. Under conditions of a total launch power of 19 dBm, a total bandwidth of 1 THz, and 101 wavelength channels, the FWM efficiency factor was computed across the entire integration domain for COI = 0 (center channel), as illustrated in Fig. 3. Here,  $f_3^{tot} = 0$ , so the axes of maximum FWM efficiency align with the frequency axes  $f_1^{tot}$  and  $f_2^{tot}$ . The FWM efficiency factor reaches its peak value of 1 at  $f_1^{tot} = 0$  and  $f_2^{tot} = 0$ , then rapidly decays as  $f_1^{tot}$  and  $f_2^{tot}$  move away from  $f_3^{tot} = 0$  [30]. It should be noted that the case presented here is a simplified scenario with  $C_r = 0$ . In the presence of ISRS, the values in the heatmap may show slight deviations, but this does not affect the subsequent analysis.

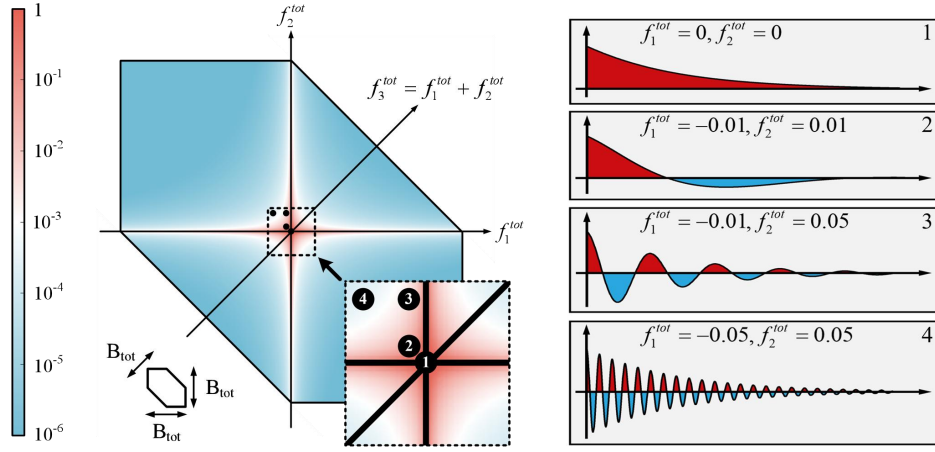


**Fig. 3.** Heatmap of the FWM efficiency factor within the EGN integration domain for a single-span WDM system with 101 wavelength channels and COI = 0. For four  $f_1^{\text{tot}}$  and  $f_2^{\text{tot}}$  (THz) positions in the figure, the waveform of the FWM efficiency factor's integrand along  $z$  is shown, with the vertical axis representing amplitude and the horizontal axis representing transmission distance  $z$ . Positive values are depicted in red, corresponding to positive integration results, while negative values are shown in blue, indicating negative integration results.

As shown in Eq. (23), calculating the FWM efficiency factor requires integration over the span length  $L_s$ . In fact, for the ISRS-considered EGN model, this integration process is one of the primary factors limiting computational speed. Fig. 3 illustrates the integration process of the FWM efficiency factor at four distinct  $f_1^{\text{tot}}$  and  $f_2^{\text{tot}}$  positions. It can be observed that as absolute values of  $(f_1^{\text{tot}} - f^{\text{tot}}) \cdot (f_2^{\text{tot}} - f^{\text{tot}})$  increases, the oscillation of the integrand becomes more pronounced. This higher oscillation frequency necessitates a larger number of samples to accurately solve the integral, thereby significantly raising computational overhead.

It could be further inferred that the oscillatory behavior of the FWM efficiency factor integrand impacts computation time differently across various COIs, with a more pronounced effect observed in edge channels. Considering the red and white regions in the computation time distribution depicted in Fig. 4 as high time-consuming areas and analyzing their proportion within the overall integration domain. It is observed that COI = -50 exhibits the highest proportion, followed by COI = 0 and COI = -25. This variation is attributed to the differing  $f^{\text{tot}}$  values corresponding to these COIs, which result in distinct distributions of  $(f_1^{\text{tot}} - f^{\text{tot}}) \cdot (f_2^{\text{tot}} - f^{\text{tot}})$ . For instance, the maximum absolute value of  $(f_1^{\text{tot}} - f^{\text{tot}}) \cdot (f_2^{\text{tot}} - f^{\text{tot}})$  is  $3/16 B_{\text{tot}}$  for COI = -25, while it reaches  $1/4 B_{\text{tot}}$  for both COI = -50 and COI = 0. For the closed-form FWM efficiency factor, computation time at each point within the integration domain is uniformly distributed. As the COI moves away from the central channel, the area of the integration domain decreases, which in turn reduces the computation time. In contrast, for the integral-form FWM efficiency factor, edge channels generally contain a larger proportion of high time-consuming areas, leading their computation time to be comparable to or even exceed that of the central channel. At an integration resolution of 1 GHz, the

total computation times for COI = 0, COI = -25, and COI = -50 in Fig. 4 are 560.2s, 492.8s, and 563.2s, respectively.

To develop an accurate approximation method for the FWM efficiency factor, the oscillatory behavior of its integrand is initially analyzed. The integrand is decomposed into three components: the SRS gain (SRS), the attenuation, and the phase mismatch factor (PMF), as described in Eq. (1).

$$\rho_s(z, f_1^{\text{tot}} + f_2^{\text{tot}} - f^{\text{tot}}) \cdot e^{i\varphi_s(f_1^{\text{tot}}, f_2^{\text{tot}}, f^{\text{tot}}, z)} = \frac{B_{\text{tot}} P_{\text{tot}} C_r L_{\text{eff}}(z) \cdot e^{-P_{\text{tot}} C_r L_{\text{eff}}(z) f^{\text{tot}}} \cdot e^{-\alpha z} \cdot e^{i4\pi^2 (f_1^{\text{tot}} - f^{\text{tot}})(f_2^{\text{tot}} - f^{\text{tot}}) [\beta_{2,3} + \beta_{1,3} (f_1^{\text{tot}} + f_2^{\text{tot}})] z}}{2 \sinh(B_{\text{tot}} P_{\text{tot}} C_r L_{\text{eff}}(z) / 2)} \cdot e^{-\alpha z} \cdot e^{i4\pi^2 (f_1^{\text{tot}} - f^{\text{tot}})(f_2^{\text{tot}} - f^{\text{tot}}) [\beta_{2,3} + \beta_{1,3} (f_1^{\text{tot}} + f_2^{\text{tot}})] z} \quad (1)$$

With  $f^{\text{tot}} = 0$ ,  $z = 0 - 100$  km, and  $C_r = 1.12$ , Fig. 5 illustrates the integrand of the FWM efficiency factor and its decomposed components at three different values of  $(f_1^{\text{tot}} - f^{\text{tot}}) \cdot (f_2^{\text{tot}} - f^{\text{tot}})$ . To facilitate explanation, only the real part of the complex result is presented in Fig. 5. The oscillatory behavior of the FWM efficiency factor integrand is attributed to the phase mismatch factor, while the SRS gain term and attenuation term remain relatively stable, forming the envelope. To derive a closed-form expression for the FWM efficiency factor, the Raman gain term was approximated, enabling the integrand to be transformed into an exponential form. Two approximation methods were utilized: one based on the Maclaurin series expansion and another on the segment approximation.

### 1) The Maclaurin Series Expansion Approximation

Define  $\zeta = P_{\text{tot}} C_r L_{\text{eff}}$ , so that Eq. (25) can be rewritten as:

$$\rho(z, f) = \frac{\zeta B_{\text{tot}} e^{-\zeta f}}{e^{\frac{\zeta B_{\text{tot}}}{2}} - e^{-\frac{\zeta B_{\text{tot}}}{2}}} \cdot e^{-\alpha z}, \quad (2)$$

By performing first-order and second-order Maclaurin series expansion on  $e^{-\zeta f}$  and  $e^{\frac{\zeta B_{\text{tot}}}{2}}$ , respectively, the following can be obtained:

$$\rho(z, f) \approx (1 - \zeta f) \cdot e^{-\alpha z}, \quad (3)$$



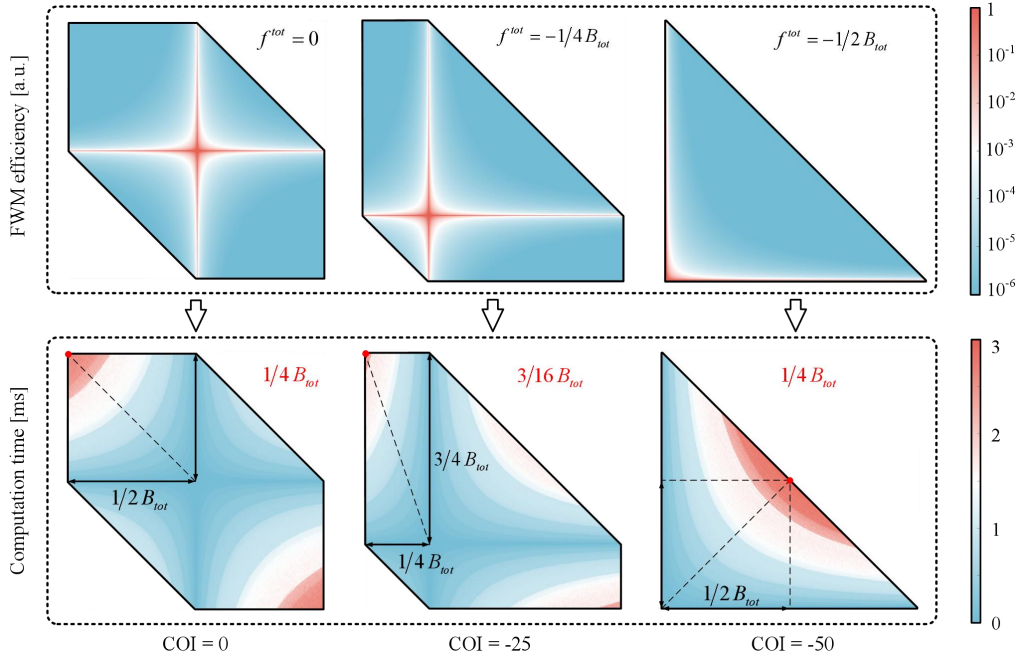


**Fig. 4.** FWM efficiency factor and computation time distribution for three different COIs in a single-span WDM system with 101 wavelength channels. Maximum absolute values of  $(f_1^{tot} - f^{tot}) \cdot (f_2^{tot} - f^{tot})$  for each COI are labeled in red text, with corresponding positions marked by red dots in the integration domain.

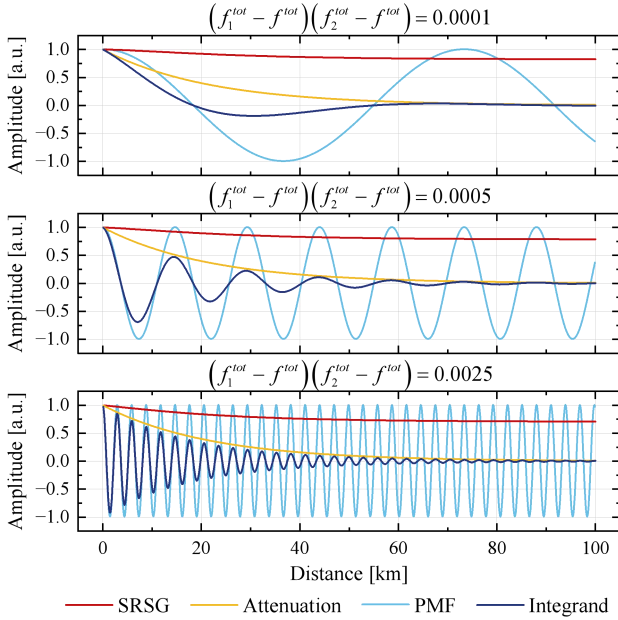


**Fig. 5.** Numerical distribution of the FWM efficiency factor integrand and its three decomposed components from  $z = 0$  to  $z = 100$  km. The overall integrand is represented by the dark blue curve, the SRS gain term by the red curve, the attenuation term by the yellow curve, and the phase mismatch factor by the light blue curve.

Substituting it into Eq. (23) and solving the integral yields:

$$\mu_s(f_1, f_2, f) \approx \eta - \frac{P_{tot} C_r (f_1 + f_2 - f)}{\alpha} \cdot \left( \eta - \frac{e^{(i\chi - 2\alpha)L_s} - 1}{i\chi - 2\alpha} \right), \quad (4)$$

$$\chi = 4\pi^2 (f_1 - f) \cdot (f_2 - f) \cdot [\beta_{2,s} + \pi\beta_{3,s} (f_1 + f_2)] \quad (5)$$

$$\eta = \frac{e^{(i\chi - \alpha)L_s} - 1}{i\chi - \alpha} \quad (6)$$

The approach utilized in this method is mentioned in [21]. In fact, this approximation method has certain limitations, which will be discussed in section C of part III.

## 2) The Segment Approximation

Over the integration range from 0 to  $L_s$ , Eq. (23) is subjected to piecewise integration into  $K$  subintervals:

$$\begin{aligned} \mu_s(f_1, f_2, f) &= \int_0^{L_s} \rho_s(z, f_1 + f_2 - f) \cdot e^{i\phi_s(f_1, f_2, f, z)} dz \\ &= \sum_{k=0}^{K-1} \int_{\frac{k}{K}L_s}^{\frac{k+1}{K}L_s} \rho_s(z, f_1 + f_2 - f) \cdot e^{i\phi_s(f_1, f_2, f, z)} dz \end{aligned} \quad (7)$$

Since the SRS gain term exhibits low variability with respect to  $z$  (as illustrated in Fig. 5), the value of  $z$  within each subinterval can be approximated by its midpoint. This allows the SRS gain term to be separated from the integral and enables the integral to be directly computed. The final results are presented in Eqs. (8)-(10).

$$\mu_s(f_1, f_2, f) \approx \sum_{k=0}^{K-1} \frac{B_{tot} P_{tot} C_r L_{eff}(z_k) e^{-P_{tot} C_r L_{eff}(z_k) (f_1 + f_2 - f)}}{2 \sinh(B_{tot} P_{tot} C_r L_{eff}(z_k) / 2)} \cdot I_k \quad (8)$$

$$I_k = \frac{e^{(i\chi - \alpha) \frac{k+1}{K} L_s} - e^{(i\chi - \alpha) \frac{k}{K} L_s}}{i\chi - \alpha} \quad (9)$$

$$z_k = \frac{k + 0.5}{K} L_s \quad (10)$$

Total segment count  $K$  is an integer and can be calculated as  $K = \lceil L_s / \Delta z \rceil$ . The smaller the sampling step  $\Delta z$ , the more accurate the approximation. However, compared to larger values of  $\Delta z$ , the computation time will increase slightly. Since this method is only slightly affected by the size of  $\Delta\rho(z)$ , the segment approximation is more accurate and has a broader applicability range compared to the Maclaurin approximation.

### III. NUMERICAL RESULTS AND DISCUSSION

#### A. Parameter Settings

In this chapter, the two proposed ISRS EGN model acceleration methods are validated. All experiments were conducted on a computer equipped with an Intel Core i7-14700KF processor (20 cores, 3.4 GHz) and 64 GB of 6400 MHz RAM. The software environment employed was MATLAB R2022b, along with the Parallel Computing Toolbox v7.7[33]. Additionally, prior to conducting the relevant experiments, we utilized the developed program to reproduce the experiment from [19], achieving consistent outcomes. In Section III(B), we assessed the computation time of the programs executed with 1-16 workers and calculated the speedup ratio. In Section III(C), the accuracy and time-saving performance of the closed-form FWM efficiency factor were validated. Accuracy was assessed by the error in the  $\eta_k$ , with its calculation method detailed in Eq. (11).

$$\eta_k \triangleq \frac{\sigma_{\text{NLL},k}^2}{P^3} \quad (11)$$

Section II-C presents two closed-form FWM efficiency factors derived using the Maclaurin approximation and the segment approximation methods, respectively. The error in the Maclaurin approximation arises from  $\mathcal{O}(P_{\text{tot}}C_rL_{\text{eff}}f)$  and  $\mathcal{O}((P_{\text{tot}}C_rL_{\text{eff}}B_{\text{tot}}/2)^2)$ , which, as shown in Eq. (12), are influenced by the value of  $\Delta\rho(z)$ . In C+L band transmission scenarios, larger values of  $B_{\text{tot}}$  generally result in larger  $\Delta\rho(z)$ , making the Maclaurin approximation potentially less accurate. Therefore, we considered two configurations,  $\Delta\rho(z) = 2.0$  and  $\Delta\rho(z) = 8.2$ , in our numerical validation to simulate ISRS influence levels in C band and C+L band scenarios, respectively. For both  $\Delta\rho(z)$  values, we examined three modulation formats—PM-QPSK, PM-16QAM, and PM-2D-Gaussian—and ten transmission distances ranging from  $1 \times 100$  km to  $10 \times 100$  km. The parameters employed in the validation experiments are summarized in Table I.

For  $\Delta\rho(z) = 2.0$ ,  $B_{\text{tot}} = 1\text{THz}, P_{\text{tot}} = 19\text{dBm}, C_r = 0.28$  was set, as shown by the dark blue dotted line in Fig. 6. For  $\Delta\rho(z) = 8.2$ , extensive experiments were not performed under a 10 THz bandwidth. Instead, by adjusting  $P_{\text{tot}}$  and  $C_r$  (with parameter values adopted from [19]), the same  $\Delta\rho(z)$  was achieved under a 1 THz bandwidth as would be under a 10 THz bandwidth. Specifically,  $B_{\text{tot}} = 1\text{THz}, P_{\text{tot}} = 19\text{dBm}, C_r = 1.12$  (red dotted line in Fig. 6) was used to approximate the scenario of  $B_{\text{tot}} = 10\text{THz}, P_{\text{tot}} = 25\text{dBm}, C_r = 0.028$  (red solid line in Fig. 6). This approach was adopted because higher bandwidth leads to a significant increase in the integration domain range, resulting in numerous points with higher oscillation frequencies, which substantially increases the computation time of the integral-form FWM efficiency factor (based on the analysis of Figs. 3 and 4). The lengthy experimental duration made it impractical to conduct experiments under a 10 THz bandwidth for all modulation formats and transmission distance configurations. It should be noted that the closed-form FWM efficiency factor

is unaffected by this issue, as it avoids integration computations entirely. The strategy of simulating the 10 THz scenario with a 1 THz bandwidth is feasible, as partial experiments conducted under  $B_{\text{tot}} = 10\text{THz}, P_{\text{tot}} = 25\text{dBm}, C_r = 0.028$  produced similar results (see Appendix C).

TABLE I  
SYSTEM PARAMETER FOR NUMERICAL VERIFICATION

Parameters	Values
Number of spans	1-10
Spans length ( $L_s$ ) [km]	100
Raman gain slope ( $C_r$ ) [1/W/km/THz]	0.28, 1.12
Attenuation ( $\alpha$ ) [dB/km]	0.2
Dispersion ( $D$ ) [ps/nm/km]	17
Dispersion slope ( $s$ ) [ps/nm <sup>2</sup> /km]	0
Nonlinear coefficient ( $\gamma$ ) [1/W/km]	1.2
Total launch power ( $P_{\text{tot}}$ ) [dBm]	19
Symbol rate ( $R$ ) [Gbaud]	10
Channel spacing [GHz]	10.1
Number of channels	101

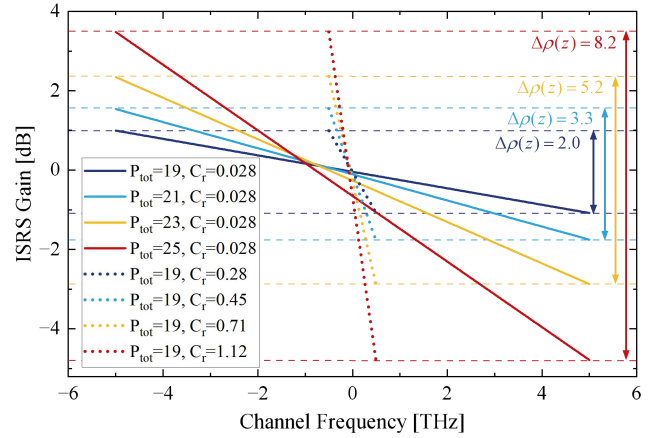


**Fig. 6.** The relationship between Raman gain and frequency after a 100 km fiber span, derived from Eq. (14) in Appendix A. Two WDM bandwidth scenarios are considered, with the 1 THz scenario represented by dotted lines and the 10 THz scenario by solid lines.

#### B. Parallel Computing Performance Evaluation

Parallel computing enhances computational efficiency without affecting the calculation results, thereby significantly reducing computation time. This work evaluated the computation time of  $\eta_k$  for the central channel using 1-16 parallel workers and calculated the speedup ratios, as illustrated in Fig. 7. As the number of workers increased, the speedup ratios across all three implementations of the FWM efficiency factors demonstrated a marked improvement. According to Amdahl's law, the speedup ratio is constrained by the serial portion of the program[34-36]. Due to the high computational complexity of the integral-form FWM efficiency factor, this program involves a larger proportion of

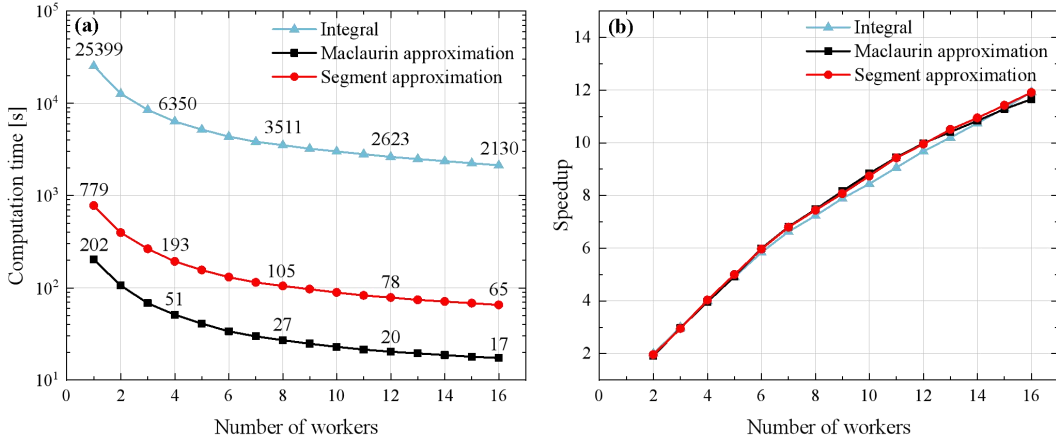


**Fig. 7.** Computation time (a) and speedup ratio (b) for calculating  $\eta_k$  of the central channel in a single-span WDM system with 101 wavelength channels using 1 to 16 parallel workers. The integral-form FWM efficiency factor is depicted in blue, the Maclaurin approximation in black, and the segment approximation in red.

parallelizable components, making it easier to achieve significant speedup. By optimizing task block sizes, the program using the closed-form FWM efficiency factor also achieved respectable parallel efficiency. Overall, with 16 workers, the computational efficiency of all three methods was significantly enhanced, yielding speedup ratios of 11.93, 11.66, and 11.91 for the integral, Maclaurin approximation, and segment approximation methods, respectively. All subsequent experiments in this work were conducted using 16 workers.

### C. Closed-Form FWM Efficiency Factor Testing

In this section, we evaluate the accuracy of the two closed-form FWM efficiency factors and their performance in reducing computation time. To ensure accuracy, the sampling step of the segment approximation method was initially set to  $\Delta z = 1$ . In subsequent experiments, we examine the impact of  $\Delta z$  on both accuracy and computation time.

Fig. 8(a) and 8(b) illustrate the results of calculating  $\eta_k$  after one span, using the integral-form and the two closed-form FWM efficiency factors with a test step size of 3. Three modulation formats were evaluated, and the integral-form FWM efficiency factor serving as the reference result. The errors of the Maclaurin approximation and segment approximation methods, relative to the reference method, are depicted in Fig. 8(c) and 8(d), respectively. When  $C_r = 0.28$ , the Maclaurin approximation exhibits a small  $\eta_k$  error, ranging from  $-0.0162$  to  $0.0091$  dB. However, at  $C_r = 1.12$ , the error increases significantly, with a maximum value of  $-0.2227$  dB. In contrast, the segment approximation is less sensitive to changes in  $\Delta\rho(z)$ , with a maximum error of only  $-0.0027$  dB even at  $C_r = 1.12$ , which is nearly negligible.

To examine the relationship between the errors of the two approximation methods and transmission distance, the experiment was repeated under 9 additional system configurations with span counts ranging from 2 to 10. As illustrated in Fig. 9(a), The MAE of  $\eta_k$  for the Maclaurin approximation method gradually increases with the number of

spans. When  $C_r = 1.12$ , the overall error is relatively high. When  $C_r = 0.28$ , although the error also accumulates, the overall magnitude remains low, indicating that the Maclaurin approximation method can still produce reasonably reliable results when  $\Delta\rho(z)$  is small. As illustrated in Fig. 9(b), the MAE of the segment approximation method does not accumulate with an increasing number of spans but exhibits a converging trend. The segment approximation method also demonstrates lower error levels, with the MAE below 0.001 dB even at  $C_r = 1.12$ .

Subsequently, to evaluate the time-saving effectiveness of the two approximation methods, the computation time of each program was tested. The single-span scenario results are illustrated in Fig. 10(a). As demonstrated by the results, the computation time for each channel using the two approximation methods generally exhibits an "arch-shaped" pattern. However, the integral-form FWM efficiency factor demonstrates higher computation times for edge channels, as discussed in the analysis of Fig. 4. Overall, the segment approximation method achieved a computation time reduction ranging from 97.0% to 98.3%. The Maclaurin approximation method further reduced computation time by several dozen seconds.

Furthermore, computation time experiments were performed under 9 additional system configurations with span counts ranging from 2 to 10, and the average computation time was calculated, as illustrated in Fig. 10(b). As the transmission distance increases, the time-saving effectiveness of both approximation methods further improves. Compared to the single-span scenario, the segment approximation method achieves an additional 0.8% reduction in computation time under the  $10 \times 100$  km span scenario. For long-distance transmission, the Maclaurin approximation method provides a more notable advantage in computation time savings, making it particularly suitable for scenarios with lower ISRS impact, such as those involving narrow bandwidth or lower launch power.

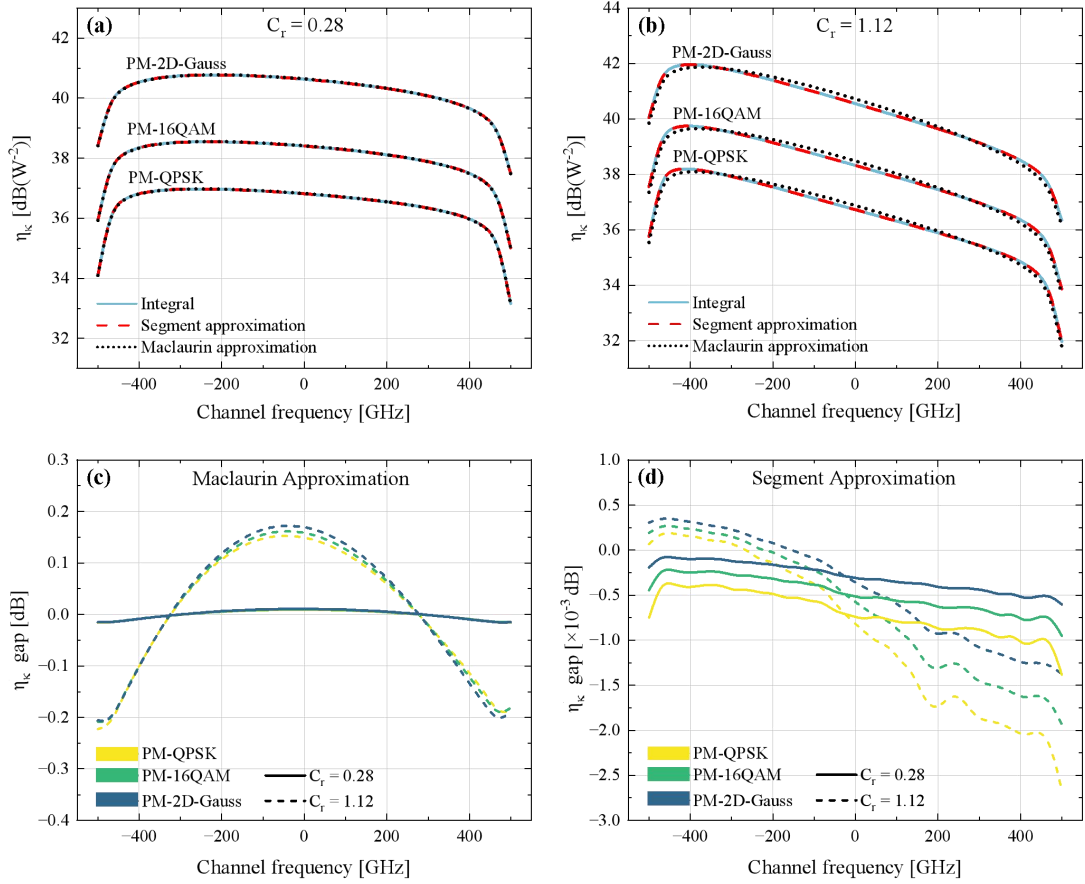


**Fig. 8.** Results of calculating  $\eta_k$  using the integral-form and two closed-form FWM efficiency factors in a single-span scenario, with (a)  $C_r = 0.28$  and (b)  $C_r = 1.12$ . The errors in  $\eta_k$  calculated using the two closed-form FWM efficiency factors are also shown: (c) based on the Maclaurin approximation and (d) based on the segment approximation.

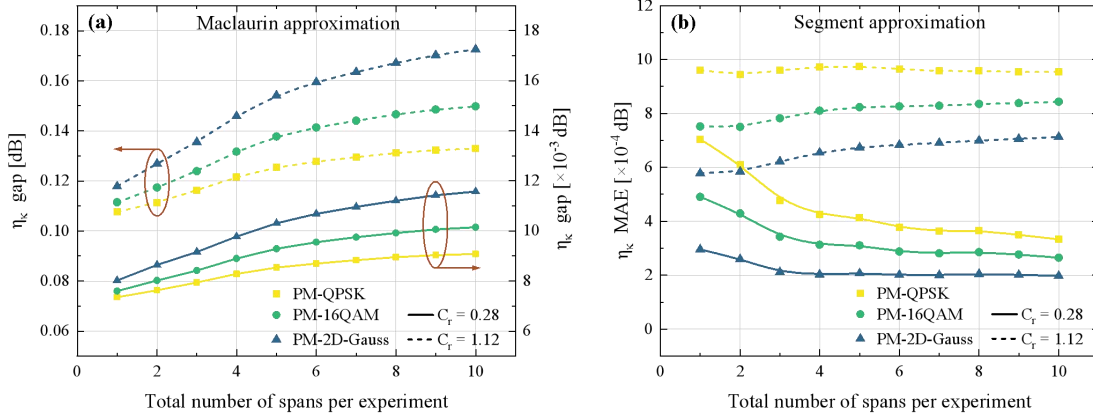


**Fig. 9.** MAE of  $\eta_k$  calculated using two closed-form FWM efficiency factors in scenarios with 1–10 spans: (a) based on the Maclaurin approximation and (b) based on the segment approximation.

In the previous experiments, a small sampling step size was selected for the segment approximation method to limit its error. Although the segment approximation method with  $\Delta z = 1$  still saves over 97% of the average computation time compared to the integral-form FWM efficiency factor, it remains slower than the Maclaurin approximation method. In fact, adjusting the value of  $\Delta z$  allows for flexible control over the accuracy and speed of the segment approximation method. As illustrated in Fig. 11(a) and 11(c), as  $\Delta z$  increases from 1

to 7, the error of the segment approximation method gradually increases, while its computation time decreases. The optimal  $\Delta z$  setting should be selected based on the specific accuracy requirements for NLI evaluation in different application scenarios. Even for applications requiring high accuracy, the value of  $\Delta z$  may be adjusted flexibly depending on the frequency of the COI. For instance, a larger  $\Delta z$  can be used for channels closer to the center frequency, as the segment approximation error is less sensitive to  $\Delta z$  in this region.



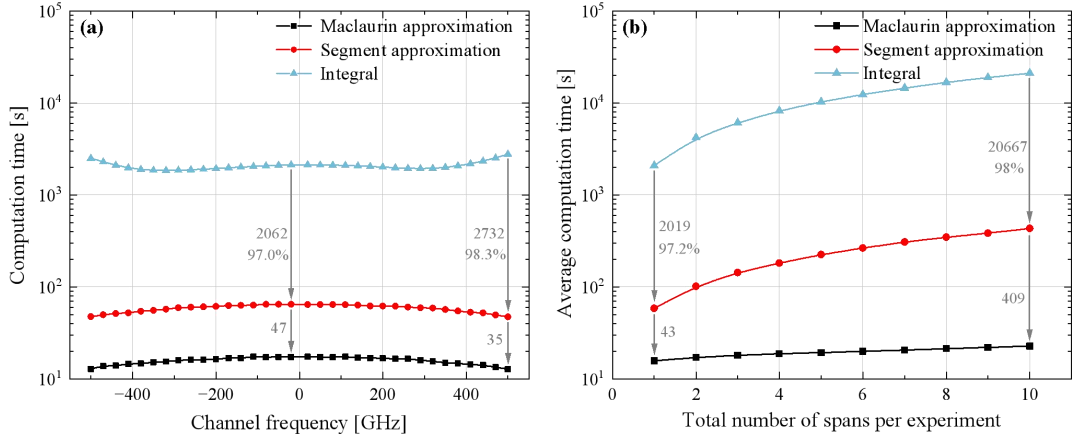


**Fig. 10.** Computation time for  $\eta_k$  evaluation across channels using the integral-form and two closed-form FWM efficiency factors in a single-span scenario, as illustrated in (a). Additionally, the average computation time in scenarios with 1–10 spans, shown in (b). A logarithmic scale is used due to the significant time difference between the integral-form and closed-form FWM efficiency factors.

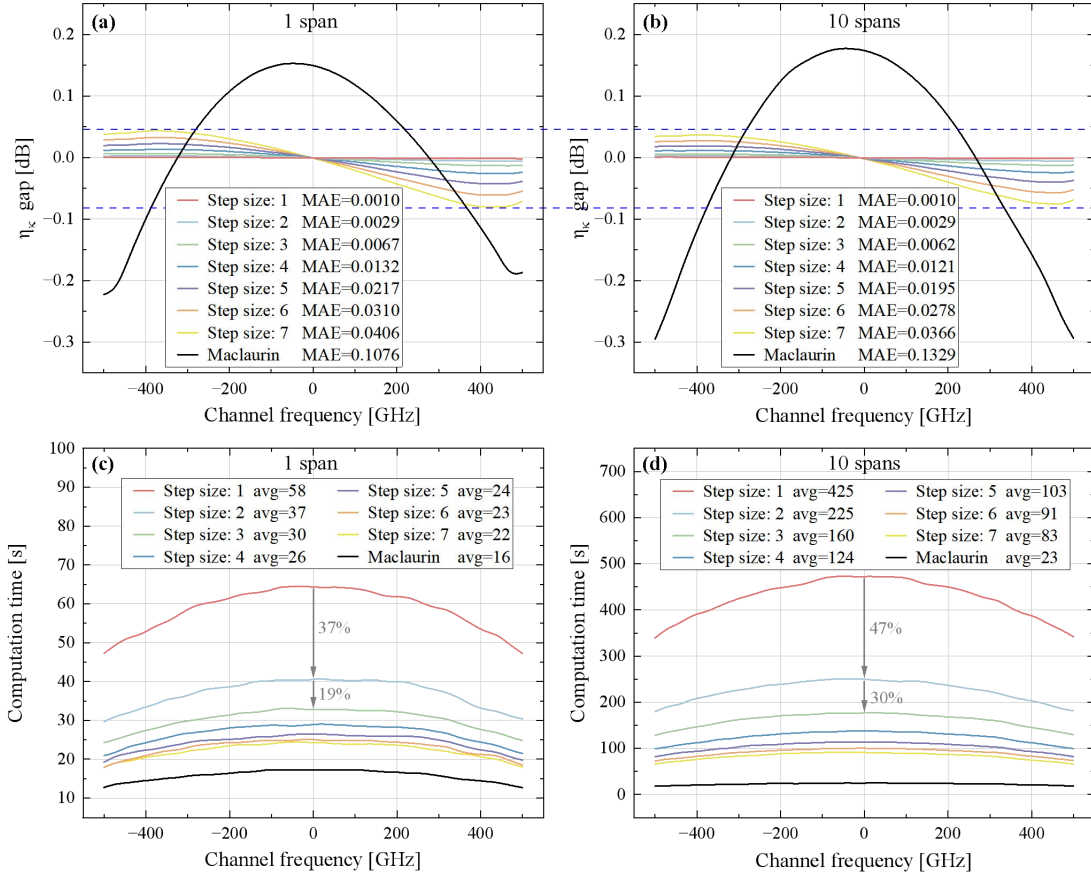


**Fig. 11.** Impact of sampling step size  $\Delta z$  (km) on the accuracy and computation time of  $\eta_k$  calculated using the segment approximation method across channels. The results shown use PM-QPSK modulation with  $c_r = 1.12$ , considering sampling steps from 1 to 7 and scenarios with 1 and 10 spans. (a) and (b) show the error for each channel; (c) and (d) show the computation time for each channel. The Maclaurin approximation method is shown as a reference.

Furthermore, experiments were performed for a 10-span scenario, as illustrated in Fig. 11(b) and 11(d). The results indicate that as transmission distance increases, the time savings achieved by increasing  $\Delta z$  also become more pronounced. For instance, in the single-span scenario, increasing  $\Delta z$  from 1 to 2 reduced computation time for the

central channel by 37%, whereas in the 10-span scenario, this reduction reached 47%. Additionally, even with a larger  $\Delta z$ , the error of the segment approximation method does not accumulate with increasing transmission distance. As illustrated in Figs. 11(a), 11(b) and 9(a), the accuracy of the Maclaurin approximation method is inadequate when  $\Delta\rho(z)$  is

large and further deteriorates with increasing transmission distance. In the single-span scenario, when  $\Delta z = 7$ , the MAE of the segment approximation is 62% lower than that of the Maclaurin approximation, and it increases to 72% in the 10-span scenario. Therefore, for scenarios with high ISRS impact levels, the segment approximation method with flexible  $\Delta z$  settings are recommended to achieve accurate and relatively fast NLI evaluation.

#### IV. CONCLUSION

This work was conducted to address the issue of the slow computation speed of the ISRS EGN model. We identified that the primary factor contributing to the long computation time in the ISRS EGN model is the integration operations required for calculating the FWM efficiency factor. By analyzing the oscillatory behavior of the integrand, we proposed an accurate approximation method and derived a closed-form expression of the FWM efficiency factor. This approach demonstrates exceptional performance, maintaining the MAE below 0.001 even under high ISRS impact levels, with no error accumulation across increasing transmission distances. The method effectively enhances the computation speed of the ISRS EGN model, achieving a computation time reduction of 97.0% to 98.3% in a single-span scenario, with additional savings observed as the transmission distance increases. Moreover, flexibly adjusting the sampling step size for different COIs and application requirements allows for further reduction in computation time. In addition, we proposed a parallel computing method, which further enhances computational efficiency by nearly 11 times, resulting in substantial time savings.

The findings of this work have substantial practical implications. When existing closed-form expressions fail to meet accuracy requirements, the proposed method enables high-precision calculations of the ISRS EGN model with relatively low computational cost. In addition, this work introduces a more efficient data generation approach for machine learning applications, facilitating the creation of larger datasets within the same time frame. Future research will extend this work to further enhance the computational speed of the ISRS EGN model.

#### APPENDIX

##### A. ISRS

Stimulated Raman scattering is a common nonlinear effects in optical fibers, causing a portion of the incident light's power is transferred from the original beam to another beam with a lower frequency[37-39]. In multi-channel transmission systems, the frequency differences between channels give rise to the ISRS effect[40-41]. [42] found that power transfer between external channels can be calculated as:

$$\Delta\rho(z)[dB] = 4.3 \cdot P_{tot} C_r L_{eff} B_{tot}, \quad (12)$$

Assuming attenuation variations are negligible, the normalized signal power distribution of spectral component  $f$  can be solved as[19]:

$$\rho(z, f) = \frac{B_{tot} P_{tot} C_r L_{eff}(z) \cdot e^{-\alpha z - P_{tot} C_r L_{eff}(z) f}}{2 \sinh\left(\frac{P_{tot} B_{tot} C_r L_{eff}(z)}{2}\right)}, \quad (13)$$

by excluding fiber attenuation from Eq. (13), the SRS gain can be obtained as:

$$SRS_G(z, f) = \frac{B_{tot} P_{tot} C_r L_{eff}(z) \cdot e^{-P_{tot} C_r L_{eff}(z) f}}{2 \sinh\left(\frac{P_{tot} B_{tot} C_r L_{eff}(z)}{2}\right)} \quad (14)$$

##### B. ISRS EGN Model

The main equation of the ISRS EGN model proposed in [19] is given in Eq. (15):

$$\sigma_{NLI, \kappa}^2 = \sum_{\kappa_1, \kappa_2, l \in \mathcal{T}_\kappa} P_{\kappa_1} P_{\kappa_2} P_{\kappa_1 + \kappa_2 - \kappa + l} \left( D_\kappa + \Phi_{\kappa_1} \cdot \delta_{\kappa_1, \kappa_1 + \kappa_2 - \kappa + l} E_\kappa \right. \\ \left. + \Phi_{\kappa_2} \delta_{\kappa_2, \kappa_2 + \kappa_1 - \kappa + l} F_\kappa + \Phi_{\kappa_1} \delta_{\kappa_1, \kappa_2} G_\kappa + \delta_{\kappa_1, \kappa_2} \delta_{\kappa_2, \kappa_2 + \kappa_1 - \kappa + l} \Psi_{\kappa_1} H_\kappa \right), \quad (15)$$

Within the integration domain, each island is delineated by  $\kappa_1$ ,  $\kappa_2$ , and  $l$ , with their combinations recorded in  $\mathcal{T}_\kappa$ :

$$\mathcal{T}_\kappa = \{(\kappa_1, \kappa_2, l) \in \{-M, \dots, M\}^2 \times \{-1, 0, 1\} : -M \leq \kappa_1 + \kappa_2 - \kappa + l \leq M\}, \quad (16)$$

The  $D_\kappa$  in Eq. (15) can be used to obtain the results for the ISRS GN model, and the correction results are calculated by  $E_\kappa$ ,  $F_\kappa$ ,  $G_\kappa$ , and  $H_\kappa$ . The specific calculation method is provided in Eqs. (17)-(21):

$$D_\kappa(\kappa_1, \kappa_2, l) = \frac{16}{27} R^2 \int_{-R/2}^{R/2} df \int_{-R/2}^{R/2} |S(f_1)|^2 df_1 \quad (17)$$

$$\cdot \int_{-R/2}^{R/2} |S(f_2)|^2 |S(f_1 + f_2 - f - lR)|^2 |Y(f_1 + \kappa_1 R, f_2 + \kappa_2 R, f + \kappa R)|^2 df_2$$

$$E_\kappa(\kappa_1, \kappa_2, l) = \frac{16}{27} R^2 \int_{-R/2}^{R/2} df \int_{-R/2}^{R/2} S(f_1) df_1 \\ \cdot \int_{-R/2}^{R/2} |S(f_2)|^2 S^*(f_1 + f_2 - f - lR) Y(f_1 + \kappa_1 R, f_2 + \kappa_2 R, f + \kappa R) df_2 \quad (18)$$

$$\cdot \int_{-R/2}^{R/2} S^*(f_1') S(f_1' + f_2 - f - lR) Y^*(f_1' + \kappa_1 R, f_2 + \kappa_2 R, f + \kappa R) df_1'$$

$$F_\kappa(\kappa_1, \kappa_2, l) = \frac{32}{81} R^2 \int_{-R/2}^{R/2} df \int_{-R/2}^{R/2} |S(f_1)|^2 df_1 \\ \cdot \int_{-R/2}^{R/2} S(f_2) S^*(f_1 + f_2 - f - lR) \cdot Y(f_1 + \kappa_1 R, f_2 + \kappa_2 R, f + \kappa R) df_2 \quad (19)$$

$$\cdot \int_{-R/2}^{R/2} S^*(f_2') S(f_1 + f_2' - f - lR) Y^*(f_1 + \kappa_1 R, f_2 + \kappa_2 R, f + \kappa R) df_2'$$

$$G_\kappa(\kappa_1, \kappa_2, l) = \frac{16}{81} R^2 \int_{-R/2}^{R/2} df \int_{-R/2}^{R/2} S(f_1) df_1 \\ \cdot \int_{-R/2}^{R/2} S(f_2) |S(f_1 + f_2 - f - lR)|^2 |Y(f_1 + \kappa_1 R, f_2 + \kappa_2 R, f + \kappa R)|^2 df_2 \quad (20)$$

$$\cdot \int_{-R/2}^{R/2} S^*(f_1') S^*(f_1 + f_2 - f_1') Y^*(f_1' + \kappa_1 R, f_1 + f_2 - f_1' + \kappa_2 R, f + \kappa R) df_1'$$

$$H_\kappa(\kappa_1, \kappa_2, l) = \frac{16}{81} R \int_{-R/2}^{R/2} df \int_{-R/2}^{R/2} S(f_1) df_1 \int_{-R/2}^{R/2} S^*(f_1') df_1' \\ \cdot \int_{-R/2}^{R/2} S(f_2) S^*(f_1 + f_2 - f - lR) \cdot Y(f_1 + \kappa_1 R, f_2 + \kappa_2 R, f + \kappa R) df_2 \quad (21)$$

$$\cdot \int_{-R/2}^{R/2} S^*(f_2') S(f_1' + f_2' - f - lR) Y^*(f_1' + \kappa_1 R, f_2 + \kappa_2 R, f + \kappa R) df_2'$$

In Eqs. (17)-(21), the calculation method for the link function  $Y$  is as follows:

$$Y(f_1, f_2, f) = \sum_{s=1}^{N_{sp}} \gamma_s \mu_s(f_1, f_2, f) \cdot e^{i4\pi^2(f_1 - f)(f_2 - f) \sum_{s=1}^{N_{sp}} (\beta_{2s} L_s + \pi(f_1 + f_2) \beta_{3s} L_s)} \\ \cdot \prod_{s=1}^{s-1} g_s^{3/2} \sqrt{\rho_s(L_s, f_1)} \sqrt{\rho_s(L_s, f_1 - f + f_2)} \sqrt{\rho_s(L_s, f_2)} \cdot \prod_{s=s+1}^{N_{sp}} g_s^{1/2} \sqrt{\rho_s(L_s, f)} \quad (22)$$

Here,  $\gamma_s$  represents the nonlinear coefficient, and  $\mu_s(f_1, f_2, f)$  reflects the efficiency of FWM. Since  $\rho_s$  accounts for the impact of ISRS,  $\mu_s$  is in integral form and can be calculated as:

$$\mu_s(f_1, f_2, f) = \int_0^{L_s} \rho_s(z, f_1 + f_2 - f) e^{i\omega_s(f_1, f_2, f, z)} dz \quad (23)$$

Where:

$$\varphi_s(f_1, f_2, f, z) = 4\pi^2(f_1 - f)(f_2 - f)[\beta_{2,s} + \pi\beta_{3,s}(f_1 + f_2)]z \quad (24)$$

$$\rho_s(z, f) = \frac{B_{tot}P_{tot}C_rL_{eff}(z)e^{-\alpha_s z - P_{tot}C_rL_{eff}(z)}}{2 \sinh(P_{tot}B_{tot}C_rL_{eff}(z)/2)} \quad (25)$$

where  $\beta_{2,s}$  and  $\beta_{3,s}$  represent the group velocity dispersion parameter and its linear slope, respectively;  $B_{tot} = (2M + 1) \cdot R$  is the total bandwidth of the WDM spectrum;  $P_{tot}$  is the total launch power of the WDM spectrum; and  $C_r$  is the linear regression slope of the normalized Raman gain spectrum.

### C. Partial 10 THz Scenario Validation

In the 10 THz scenario, the errors and MAE of  $\eta_k$  calculated using the Maclaurin approximation and the segment approximation methods are presented in Fig. 12. The segment approximation method evaluated using sampling steps ranging from 1 to 7. Detailed system parameters are listed in Table 2. The numerical results are similar to Fig. 11(a).

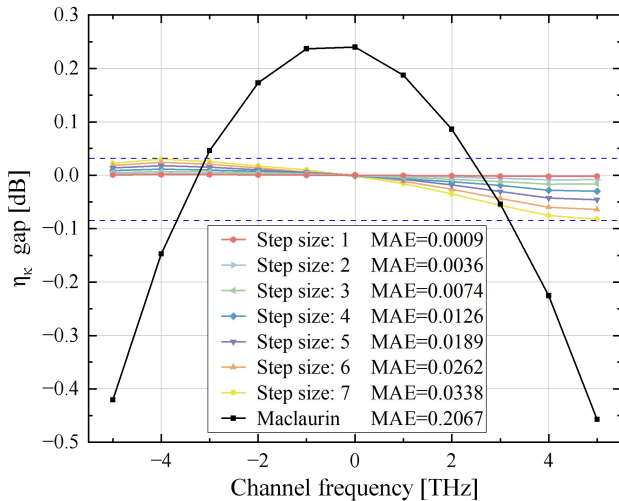


**Fig. 12.** Accuracy validation of Maclaurin approximation and segment approximation in the 10 THz bandwidth Scenario.

TABLE II  
SYSTEM PARAMETER FOR THE 10THZ SCENARIO

Parameters	Values
Number of spans	1
Spans length ( $L_s$ ) [km]	100
Raman gain slope ( $C_r$ ) [1/W/km/THz]	0.028
Attenuation ( $\alpha$ ) [dB/km]	0.2
Dispersion ( $D$ ) [ps/nm/km]	17
Dispersion slope ( $s$ ) [ps/nm <sup>2</sup> /km]	0.067
Nonlinear coefficient ( $\gamma$ ) [1/W/km]	1.2
Total launch power ( $P_{tot}$ ) [dBm]	25
Symbol rate ( $R$ ) [Gbaud]	100
Channel spacing [GHz]	101
Number of channels	101

### ACKNOWLEDGMENT

This work was supported in part by National Key Research and Development Program of China (2022YFB2903303) and National Natural Science Foundation of China (No. 62141505, 61367007 and 62371064).

### REFERENCES

- [1] K. Kılınçarslan and S. E. Karlık, "Combined impact of SRS, FWM and ASE noise in UDWDM/DWDM long-haul communication systems using EDFAs," *Opt. Laser Technol.*, vol. 157, Jan. 2023, Art. no. 108695, doi: 10.1016/j.optlastec.2022.108695.
- [2] K. Kimura, T. Kobayashi, S. Shimizu, M. Nakamura, T. Kazama, M. Abe, T. Umeki, A. Kawai, F. Hamaoka, and Y. Miyamoto, "System performance estimation accounting for stimulated Raman scattering in 14.1-THz bandwidth S+C+L inline-amplified transmission," *J. Lightw. Technol.*, vol. 42, no. 24, pp. 8616–8627, Dec. 2024, doi: 10.1109/JLT.2024.3434725.
- [3] A. Raeesi, H. Rabbani, L. Beygi, and S. Zokaee, "Discretized Gaussian model for nonlinear noise in elastic optical networks," *Optics Communications*, vol. 460, Apr. 2020, Art. no. 125002, doi: 10.1016/j.optcom.2019.125002.
- [4] U. C. De Moura, D. Zibar, A. Margareth Rosa Brusin, A. Carena, and F. Da Ros, "Fiber-agnostic machine learning-based Raman amplifier models," *J. Lightw. Technol.*, vol. 41, no. 1, pp. 83–95, Jan. 2023, doi: 10.1109/JLT.2022.3210769.
- [5] Z. Liang, B. Chen, Y. Lei, G. Liga, and A. Alvarado, "Analytical model of nonlinear fiber propagation for general dual-polarization four-dimensional modulation formats," *J. Lightw. Technol.*, vol. 42, no. 2, pp. 606–620, Jan. 2024, doi: 10.1109/JLT.2023.3316836.
- [6] D. Wang, Y. Song, Y. Zhang, X. Jiang, J. Dong, F. N. Khan, T. Sasai, S. Huang, A. P. L. Lau, M. Tornatore, and M. Zhang, "Digital twin of optical networks: a review of recent advances and future trends," *J. Lightw. Technol.*, vol. 42, no. 12, pp. 4233–4259, Jun. 2024, doi: 10.1109/JLT.2024.3401419.
- [7] M. A. Amirabadi, S. A. Nezamalhosseini, M. H. Kahaei, and A. Carena, "Deep learning-based classification for QoT estimation in SMF and FMF links," *J. Lightw. Technol.*, pp. 1–17, 2024, doi: 10.1109/JLT.2024.3451242.
- [8] M. Torbatian, D. Lavery, M. Osman, D. Yao, D. S. Millar, Y. Gao, A. Kakkar, Z. A. El-Sahn, C. Daggart, A. E. Morra, N. Abughalieh, S. Yang, X. Chen, R. Maher, H. Sun, K.-T. Wu, and P. Kandappan, "Performance oriented DSP for flexible long haul coherent transmission," *J. Lightw. Technol.*, vol. 40, no. 5, pp. 1256–1272, Mar. 2022, doi: 10.1109/JLT.2021.3134155.
- [9] P. Poggiolini, G. Bosco, A. Carena, V. Curri, Y. Jiang, and F. Forghieri, "The GN-model of fiber non-linear propagation and its applications," *J. Lightw. Technol.*, vol. 32, no. 4, pp. 694–721, Feb. 2014, doi: 10.1109/JLT.2013.2295208.
- [10] D. Semrau, E. Sillekens, P. Bayvel, and R. I. Killey, "Modeling and mitigation of fiber nonlinearity in wideband optical signal transmission," *J. Opt. Commun. Netw.*, vol. 12, no. 6, pp. C68–C76, June 2020, doi: 10.1364/JOCN.382267.
- [11] P. Poggiolini and Y. Jiang, "Recent advances in the modeling of the impact of nonlinear fiber propagation effects on uncompensated coherent transmission systems," *J. Lightw. Technol.*, vol. 35, no. 3, pp. 458–480, Feb. 2017, doi: 10.1109/JLT.2016.2613893.
- [12] H. Rabbani, H. Hosseinianfar, H. Rabbani, and M. Brandt-Pearce, "Analysis of nonlinear fiber Kerr effects for arbitrary modulation formats," *J. Lightw. Technol.*, vol. 41, no. 1, pp. 96–104, Jan. 2023.
- [13] R. Dar, M. Feder, A. Mecozzi, and M. Shtaif, "Accumulation of nonlinear interference noise in fiber-optic systems," *Opt. Express*, vol. 22, no. 12, pp. 14199–14211, Jun. 2014, doi: 10.1364/OE.22.014199.
- [14] A. Carena, G. Bosco, V. Curri, P. Poggiolini, and F. Forghieri, "Impact of the transmitted signal initial dispersion transient on the accuracy of the GN-model of non-linear propagation," in *Proc. of ECOC 2013*, London, U.K., Sep. 2013, paper Th.1.D.4, doi: 10.1049/cp.2013.1515.
- [15] P. Serena and A. Bononi, "On the accuracy of the Gaussian nonlinear model for dispersion-unmanaged coherent links," in *Proc. of ECOC 2013*, London, U.K., Sep. 2013, paper Th.1.D.3, doi: 10.1049/cp.2013.1514.
- [16] R. Dar, M. Feder, A. Mecozzi, and M. Shtaif, "Properties of nonlinear noise in long, dispersion-uncompensated fiber links," *Opt. Express*, vol.

- 21, no. 22, pp. 25685–25699, Nov. 2013, doi: 10.1364/OE.21.025685.
- [17] A. Carena, G. Bosco, V. Curri, Y. Jiang, P. Poggiolini, and F. Forghieri, “EGN model of non-linear fiber propagation,” *Opt. Express*, vol. 22, no. 13, pp. 16335–16362, Jun. 2014, doi: 10.1109/JLT.2013.2246543.
- [18] N. Guo, G. Shen, N. Deng, and B. Mukherjee, “Can channel power optimization with GSNR flatness maximize capacities of C+L-band optical systems and networks?” *J. Lightw. Technol.*, vol. 42, no. 16, pp. 5506–5521, Aug. 2024, doi: 10.1109/JLT.2024.3395620.
- [19] H. Rabbani, G. Liga, V. Oliari, L. Beygi, E. Agrell, M. Karlsson, and A. Alvarado, “A general analytical model of nonlinear fiber propagation in the presence of Kerr nonlinearity and stimulated Raman scattering,” Jun. 2020, *arXiv: 1909.08714v2*.
- [20] D. Semrau, R. Killey, and P. Bayvel, “Achievable rate degradation of ultra-wideband coherent fiber communication systems due to stimulated Raman scattering,” *Opt. Express*, vol. 25, no. 12, pp. 13024–13034, Jun. 2017, doi: 10.1364/OE.25.013024.
- [21] D. Semrau, R. I. Killey, and P. Bayvel, “A closed-form approximation of the Gaussian noise model in the presence of inter-channel stimulated Raman scattering,” *J. Lightw. Technol.*, vol. 37, no. 9, pp. 1924–1936, May 2019, doi: 10.1109/JLT.2019.2895237.
- [22] D. Semrau, E. Sillekens, R. I. Killey, and P. Bayvel, “A modulation format correction formula for the Gaussian noise model in the presence of inter-channel stimulated Raman scattering,” *J. Lightw. Technol.*, vol. 37, no. 19, pp. 5122–5131, Oct. 2019, doi: 10.1109/JLT.2019.2929461.
- [23] M. R. Zefreh, F. Forghieri, S. Piciaccia, and P. Poggiolini, “Accurate closed-form real-time EGN model formula leveraging machine-learning over 8500 thoroughly randomized full C-band systems,” *J. Lightw. Technol.*, vol. 38, no. 18, pp. 4987–4999, Sep. 2020, doi: 10.1109/JLT.2020.2997395.
- [24] J. Müller, T. Fehenberger, S. K. Patri, K. Kaeval, H. Griesser, M. Tikas, and J.-P. Elbers, “Estimating quality of transmission in a live production network using machine learning,” in *Proc. of OFC 2021*, Washington, Jun. 2021, p. Tu1G.2. doi: 10.1364/OFC.2021.Tu1G.2.
- [25] J. Müller, S. K. Patri, T. Fehenberger, H. Griesser, J.-P. Elbers, and C. Mas-Machuca, “QoT estimation using EGN-assisted machine learning for multi-period network planning,” *J. Opt. Commun. Netw.*, vol. 14, no. 12, pp. 1010–1019, Dec. 2022, doi: 10.1364/JOCN.472632.
- [26] H. Buglia, M. Jarmolovičius, A. Vasylychenkova, E. Sillekens, L. Galdino, R. I. Killey, and P. Bayvel, “A closed-form expression for the Gaussian noise model in the presence of inter-channel stimulated Raman scattering extended for arbitrary loss and fibre length,” *J. Lightw. Technol.*, vol. 41, no. 11, pp. 3577–3586, Jun. 2023, doi: 10.1109/JLT.2023.3256185.
- [27] L. Al-Tarawneh, A. Alqatawneh, A. Tahat, and O. Saraereh, “Evolution of optical networks: from legacy networks to next-generation networks,” *J. Opt. Commun.*, vol. 44, no. s1, pp. s955–s970, Feb. 2024, doi: 10.1515/joc-2020-0108.
- [28] Z. Ouyang, X. Chen, Z. Liu, X. Chen, and Z. Zhu, “Overview of ML-aided QoT estimation in optical networks: a perspective of model generalization”, in *Proc. of ICCT 2024*, Chengdu, Sep. 2024.
- [29] F. N. Khan, “Machine learning-enabled intelligent fiber-optic communications: major obstacles and the way forward,” *IEEE Commun. Mag.*, vol. 61, no. 4, pp. 122–128, Apr. 2023, doi: 10.1109/MCOM.003.2200186.
- [30] P. Poggiolini, “The GN model of non-linear propagation in uncompensated coherent optical systems,” *J. Lightw. Technol.*, vol. 30, no. 24, pp. 3857–3879, Dec. 2012, doi: 10.1109/JLT.2012.2217729.
- [31] M. Pricopi and T. Mitra, “Task scheduling on adaptive multi-core,” *IEEE Trans. Comput.*, vol. 63, no. 10, pp. 2590–2603, Oct. 2014, doi: 10.1109/TC.2013.115.
- [32] L. Yavits, A. Morad, and R. Ginosar, “The effect of communication and synchronization on Amdahl’s law in multicore systems,” *Parallel Computing*, vol. 40, no. 1, pp. 1–16, Jan. 2014, doi: 10.1016/j.parco.2013.11.001.
- [33] D. N. Varsamis, C. Talagkozis, P. A. Mastorocostas, E. Outsios, and N. P. Karampetakis, “The performance of the MATLAB Parallel Computing Toolbox in specific problems,” in *Proc. of FedC/SIS 2012*, Wroclaw, Sep. 2012, pp. 587–593.
- [34] S. Tang, B.-S. Lee, and B. He, “Speedup for multi-level parallel computing,” in *2012 IEEE 26th International Parallel and Distributed Processing Symposium Workshops & PhD Forum*, Shanghai, May 2012, pp. 537–546. doi: 10.1109/IPDPSW.2012.72.
- [35] A. S. Filipchenko, “Method for determining the acceleration of a parallel specialised computer system based on Amdahl’s law,” Jan. 2024, *arXiv: 2401.16975*.
- [36] M. A. N. Al-hayanni, F. Xia, A. Rafiev, A. Romanovsky, R. Shafik, and A. Yakovlev, “Amdahl’s law in the context of heterogeneous many-core systems – a survey,” *IET Comput. Digit. Techn.*, vol. 14, no. 4, pp. 133–148, Jul. 2020, doi: 10.1049/iet-cdt.2018.5220.
- [37] C. Lasagni, P. Serena, A. Bononi, and J.-C. Antona, “A generalized Raman scattering model for real-time SNR estimation of multi-band systems,” *J. Lightw. Technol.*, vol. 41, no. 11, pp. 3407–3416, Jun. 2023, doi: 10.1109/JLT.2023.3250751.
- [38] Y. Teng, H. Yang, Q. Yao, R. Gu, Z. Sun, A. Xu, F. Liu, and J. Zhang, “SRS-proactive-aware resource allocation based on all-optical wavelength converters in C+L band optical networks,” *J. Lightw. Technol.*, vol. 42, no. 19, pp. 6632–6646, Oct. 2024, doi: 10.1109/JLT.2024.3411886.
- [39] M. Cantono, D. Pileri, A. Ferrari, C. Catanese, J. Thouras, J.-L. Augé, and V. Curri, “On the interplay of nonlinear interference generation with stimulated Raman scattering for QoT estimation,” *J. Lightw. Technol.*, vol. 36, no. 15, pp. 3131–3141, Aug. 2018, doi: 10.1109/JLT.2018.2814840.
- [40] D. Semrau, E. Sillekens, R. I. Killey, and P. Bayvel, “Modelling the delayed nonlinear fiber response in coherent optical communications,” *J. Lightw. Technol.*, vol. 39, no. 7, pp. 1937–1952, Apr. 2021, doi: 10.1109/JLT.2020.3046998.
- [41] M. Zirngibl, “Analytical model of Raman gain effects in massive wavelength division multiplexed transmission systems,” *Electron. Lett.*, vol. 34, no. 8, pp. 789–790, Apr. 1998, doi: 10.1049/el:19980555.
- [42] D. Semrau, R. I. Killey, and P. Bayvel, “The Gaussian noise model in the presence of inter-channel stimulated Raman scattering,” *J. Lightwave Technol.*, vol. 36, no. 14, pp. 3046–3055, Jul. 2018, doi: 10.1109/JLT.2018.2830973.